



Molecular dynamics based study and characterization of deformation mechanisms near a crack in a crystalline material

Jiaxi Zhang, Somnath Ghosh*

Department of Civil Engineering, Johns Hopkins University, 203 Latrobe, 3400 N. Charles Street, Baltimore, MD 21218, United States

ARTICLE INFO

Article history:

Received 21 January 2013

Received in revised form

11 April 2013

Accepted 12 April 2013

Available online 23 April 2013

Keywords:

Deformation mechanisms

Crack-tip plasticity

Dislocation

Cohesive zone model

Molecular dynamics

ABSTRACT

Modeling crack propagation in crystalline materials is a challenging enterprise due to complexities induced by the interaction of the crack with various deformation mechanisms such as dislocation, micro twin, stacking faults etc.. As a first step toward the development of physics-based models of deformation in the presence of a crack, this paper proposes a comprehensive approach based on molecular dynamics simulations of a crystalline material with an embedded crack. The MD-based framework invokes a sequence of four tasks to accomplish the overall goal, viz. (i) MD simulation, (ii) characterization of atomic-level crack and deformation mechanisms, (iii) quantification of atomic-level deformation mechanisms and crack, and (iv) response analysis. Effective characterization methods like CNA, DXA and deformation gradient analysis followed by quantification are able to delineate the crack length/opening, dislocation structure and microtwins at a high resolution. Interactions of the crack with the dislocation networks and microtwins under mode I loading conditions are investigated for different lattice orientations. Crystal orientation has significant effect on the mechanisms activation and evolution. An important study is made through partitioning of the total energy into recoverable elastic energy, defect energy and inelastic dissipation, and correlating them with deformation characteristics such as dislocation density and twin volume fraction. Finally, a simple mechanistic model of deformation is developed, which associates dislocation density evolution with the stress–strain response in a crystalline material in the presence of a crack. Results show good quantitative agreement of material softening and hardening behavior with direct MD simulation results. The model can be further used to estimate the range of strain-rates that may be applied for physically meaningful MD simulations.

© 2013 Elsevier Ltd. All rights reserved.

1. Introduction

Accurate modeling of fatigue and failure in metals and alloys inherently involves coupling of multiple spatial scales ranging from the atomic domains of cracks, voids and associated deformation mechanisms to those of grains and grain boundaries and polycrystalline aggregates. The nucleation of these mechanisms, including dislocation, micro twin and their interactions with other defects such as voids and grain boundaries are major factors which determine the ductile fracture behavior. At the macroscopic level, cohesive zone model (CZM) are often implemented with crystal plasticity finite element method (CPFEM) to describe the gradual separation process by phenomenological traction–displacement relations

* Corresponding author. Tel.: +1 410 516 7833; fax: +1 410 516 7473.

E-mail address: sghosh20@jhu.edu (S. Ghosh).

(Tvergaard and Hutchinson, 1992; Costanzo and Allen, 1995; Camacho and Ortiz, 1996; Klein and Gao, 1998). Although such interpretations of the fracture process enjoy ease of numerical implementation, especially due to absence of crack-tip singularity, they face significant challenges. Parameters fitted using macroscopic experimental data are non-unique since heterogeneous, microstructure dependent crack-growth and associated mechanisms at the sub-micron level are not captured. Clearly, there is a considerable need for better understanding and quantitative representation of the crack-growth process, along with the evolution of associated plastic deformation at the atomistic scales of inception. Special homogenization methodologies must then be developed to propose unified plasticity and crack propagation relations at the scale of single crystals, that can be incorporated in crystal plasticity finite element models. Such homogenization techniques are currently scarce in the literature primarily because of discrepancies in the representation of mechanisms at discrete and continuum scales, as well as difference in temporal scales. This reinforces the need to develop a systematic framework involving characterization and representation at individual scales, and consequent scale-bridging.

With the increase of computational power, atomistic simulations with methods like molecular dynamics (MD) are being widely used to investigate evolution and interaction of damage mechanisms. These methods have the capability of representing defect structures and other deformation mechanisms at a high resolution. Recently a 320 billion atom simulation, using the Lennard–Jones two body potential was conducted on the BlueGene/L in Kadau et al. (2006), reaching micron length scales. Zhou et al. (1996) have conducted MD simulations with 35 million atoms to study ductile fracture in copper using the embedded atom method or EAM potential. As one of the earlier studies on large scale crack propagation, they exhibit emission of dislocation loops from the crack tip, causing blunting due to the interaction of crack and plastic deformations.

The dynamics of crack propagation and different deformation mechanisms in metals have been studied by atomistic simulations in great detail for both transgranular and intergranular cracks in Buehler et al. (2004), Knap and Sieradzki (1999), Yamakov et al. (2006) and Zhu et al. (2004). These studies have investigated the plastic deformation process at crack tip, focusing on the structure of nucleated dislocations networks, formation of dislocation junctions and deformation twinning. MD simulations display high heterogeneity of dislocation distribution near crack tip. This is consistent with transmission electron microscopy observations in Ohr (1985) and Horton and Ohr (1982). Studies have also been conducted on nano-crystalline materials and grain boundary systems (Swygenhoven et al., 2004; Yamakov et al., 2002; Tschopp and McDowell, 2008). While these studies provide important insight into the evolution of plastic mechanisms, the analyses predominantly provide a qualitative perspective. Quantitative description and correlation between the deformation mechanisms and mechanical response, though important are mostly unresolved.

A number of studies have attempted to extract cohesive zone model parameters from atomistic simulations results. Bicrystal interfaces under tensile and shear loads have been studied in Spearot et al. (2004), while a single crystal containing a crack under mixed-mode loads has been investigated in Zhou et al. (2008). Both studies derive traction-displacement relations from the atomistic simulations. Decohesion of grain boundary systems under hydrostatic loading have been explored in Yamakov et al. (2006), revealing the appearance of brittle debonding and ductile crack propagation associated with micro-twin formation. Their local stresses along the interface show good agreement with models in Rice (1992) and Tadmor and Hai (2003). Quasi-continuum based formulation with cohesive potentials have been implemented in Liu et al. (2008) for modeling crack propagation process. Most of these works present direct traction-displacement relationships, with displacements in the nanometer scale. However the length scale of the decohesion process in crystalline metals is related to the plastic zone, which is much larger than the nanometer scale. Additionally, energy dissipation due to plastic deformation is a major contributor to the energy release-rate for ductile fracture. Therefore energy-based methods with quantification of plastic deformation mechanisms are perceived to better present the crack evolution process.

This paper is a first step in developing continuum level plasticity-damage models, based on quantitative information of deformation mechanisms obtained from molecular dynamics (MD) simulations of a crystalline material with an embedded crack. It is focused on constructing a methodology for characterization of crack propagation and associated deformation mechanisms in atomistic simulations, that can be then harnessed in the development of continuum models. The MD platform is selected over other candidate methods such as discrete dislocation dynamics (DDD) to provide high-resolution descriptions of the structure of mechanisms and defects, e.g. crack face, twins and grain boundaries. The MD model is described in Section 2. The MD-based framework invokes a sequence of four tasks to accomplish the overall goal, viz. (i) MD simulation, (ii) characterization of atomic-level crack and deformation mechanisms, (iii) quantification of atomic-level deformation mechanisms and crack, and (iv) response analysis. The characterization and quantification approaches, described in Section 3 focus on full/partial dislocations, twinning and micro cracks. In Section 4, the paper analyzes lattice orientation and loading direction dependent evolution of deformation mechanisms in single crystal Nickel (fcc) under uniaxial tension. Partitioning of energy in the molecular ensemble is performed in Section 5 to delineate energy contribution from different deformation mechanisms. Finally in Section 6 a simple mechanistic model is developed, accounting for the deformation mechanisms in a crystalline material in the presence of a crack. Comparison of the model with direct MD simulation results demonstrate the potential of the proposed approach.

2. Molecular dynamics model of single crystal nickel with an embedded crack

A molecular dynamics (MD) simulation model of single crystal nickel (Ni) with an embedded crack is developed to investigate nano-scale crack-tip deformation mechanisms that govern crack evolution in the crystalline lattice. The model

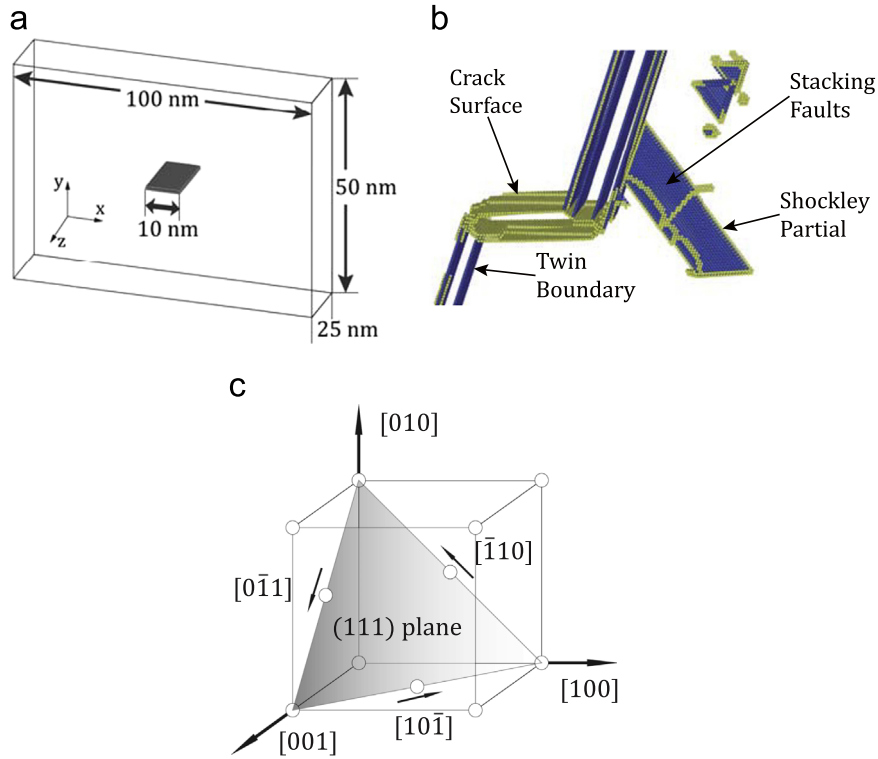


Fig. 1. (a) Representative dimensions of the MD simulation box with an embedded crack (only atoms on the crack surface are shown), (b) characteristic plastic deformation mechanisms evolving in MD simulation, colored by the local atom structure and (c) one of the four slip planes and corresponding slip directions for Ni.

system of a face centered cubic structured (lattice constant 3.52 Å) single crystal nickel with an embedded center crack is shown in Fig. 1(a). The four slip planes and corresponding slip directions for single crystal Nickel are shown in Fig. 1(c). The MD simulation box is approximately 100 nm × 50 nm × 25 nm in the x, y, z directions respectively. The dimension in the z direction is taken to be comparable to those in the x and y directions to ensure that the resistance to the dislocation motion due to image forces is sufficiently small. The initial crack is assumed to be of length 10 nm with a maximum opening of 1 nm and continuous in the z direction. Slip system interaction is a major mechanism of crystal lattice hardening. The dimension of the simulation box in the z direction is sufficiently large to ensure accurate three-dimensional dislocation evolution in all active slip systems at the crack tip. Three high symmetry lattice orientations are studied for this simulation box, viz.

1. Orientation 1: $x \rightarrow [\bar{1}10]$, $y \rightarrow [111]$, $z \rightarrow [11\bar{2}]$
2. Orientation 2: $x \rightarrow [11\bar{2}]$, $y \rightarrow [111]$, $z \rightarrow [1\bar{1}0]$
3. Orientation 3: $x \rightarrow [100]$, $y \rightarrow [010]$, $z \rightarrow [001]$

Fig. 1(b) shows a few key characteristic plastic deformation mechanisms evolving with overall deformation in the MD simulation.

2.1. Boundary and loading conditions

Periodic boundary conditions are applied on faces of the simulation box. Translational symmetry in the z direction extends the crack infinitely in this direction. The simulation box is subjected to an applied constant engineering strain-rate $\dot{\epsilon}_{yy} = \dot{\epsilon}_c$ in the y direction. In MD simulations, this strain-rate control is realized by requiring atoms to move via affine transformation, prior to time-step integration of the governing equations. Under this condition, an atom at a position $\mathbf{r}_i = (x, y, z)$ in the system is displaced by $\Delta \mathbf{u}$ in a time-step Δt before integrating the dynamic equilibrium equations, which is:

$$\Delta \mathbf{u} = (\Delta u_x, \Delta u_y, \Delta u_z) = (0, \Delta t \dot{\epsilon}_c y, 0) \quad (1)$$

Simultaneously, the pressure in the x and z directions are kept to $p_x = 0$ and $p_z = 0$ by a *NPT* canonical ensemble to represent uniaxial tension (Berendsen et al., 1984).

Table 1

Comparison of values of parameters related to different deformation mechanisms obtained by different methods: (a) experiments (Bulatov and Cai, 2006), (b) ab-initio calculations (Kibey et al., 2007), (c) EAM potential (Angelo et al., 1995; Chassagne et al., 2011), and (d) MEAM potential (Baskes, 1992).

Parameters	Experiment (a)	Ab initio (b)	EAM (c)	MEAM (d)
Lattice constant (Å)	3.52	3.52	3.52	3.52
γ_{ssf} (mJ/m ²)	125	110	88	125
γ_{usf} (mJ/m ²)		273	212	
γ_{st} (mJ/m ²)	43	55	50	
γ_{ut} (mJ/m ²)		324	159	

2.2. Atomic interaction potential

The interaction between nickel atoms is calculated by a multi-body potential function described by the embedded-atom method or EAM (Daw and Baskes, 1984). This potential is found to be appropriate for most transition metal systems. The EAM potential developed in Angelo et al. (1995) is used in the present work. While the computational cost with the EAM potential is about twice that with the Lennard–Jones potential, it has been shown to be significantly more accurate in predicting the general stacking fault energy functions, e.g. in Zimmerman et al. (2000), needed for modeling plastic deformation. The modified embedded-atom method (MEAM) has been developed in Baskes (1992) for application to a much broader class of material system including alloys and those with covalent bonds. This method includes additional directional bonding dependent terms. However, for pure nickel, this method is about 10 times more computationally expensive than the EAM potential, while their accuracies are sufficiently comparable. This is demonstrated for various variables shown in Table 1. Hence the EAM potential is considered to be adequate for the MD simulations in this paper.

In the EAM, an atom is viewed as being embedded in a host lattice consisting of all other atoms in the ensemble. The “embedding energy” of an atom i is a function of the electron density before it is included. The functional form of the EAM potential energy of an atom i is given as

$$U_i = \mathcal{F}_\alpha \left(\sum_{j \neq i} \rho_\beta(r_{ij}) \right) + \frac{1}{2} \sum_{j=1, j \neq i}^N \phi_{ij}(r_{ij}) \quad (2)$$

The first term is an embedding function that represents the energy required to place an atom i of type α into the electron cloud. The electron cloud density is a summation over many atoms, usually limited by a cutoff radius. In the embedding energy function \mathcal{F}_α , ρ_β is the contribution to the electron charge density from atom j of type β at the location of atom i . It is a function of the distance r_{ij} between atoms i and j within a cutoff distance. The second term is a short-range electrostatic pair-wise potential that is a function of the distance r_{ij} between atoms i and j . For a single element system, three scalar functions must be specified, viz. the embedding function, a pair-wise interaction function, and the electron cloud contribution function.

The study of plastic deformation mechanisms associated with crack propagation in metallic systems requires accurate values of the stable and unstable stacking-fault energies γ_{ssf} and γ_{usf} respectively, and the stable and unstable twinning energies γ_{st} and γ_{ut} respectively. These values have been shown to have significant effects on the plastic behavior of metals in Swygenhoven et al. (2004) and Tadmor and Bernstein (2004). Good agreement has been shown between values of these variables obtained by experiments, ab-initio calculations and EAM potential based calculations. Comparison of the lattice constant, stable and unstable stacking fault energy and twinning energy are shown in Table 1 with generally satisfactory results. The EAM potential in this work is however found to underestimate the values of γ_{ssf} and γ_{ut} when compared with MEAM and ab-initio based calculations, as seen in Table 1. Larger stable stacking fault (ssf) energy, obtained from the MEAM potential, is expected to result in a smaller separation between the leading and trailing partial dislocation cores, i.e. a smaller stacking fault area. This reduces the energy barrier for the cross-slip mechanism, which induces more cross-slip with the MEAM potential. Unstable twin energy, corresponding to the energy barrier for twin formation, has insignificant effect on dislocation behavior. Larger γ_{ut} , derived from ab-initio calculations, increases the energy barrier of twin formation. A comparison of twins formed by the present potential and another EAM potential developed in Mishin et al. (1999) with $\gamma_{\text{ut}} = 357$ meV shows twin formation with both potentials. However, the twin volume fraction with the potential in Mishin et al. (1999) is slightly smaller. Thus it may be concluded that the deformation mechanisms are not expected to be qualitatively affected by the differences in stable stacking fault energy and unstable twin energy, exhibited in the table.

A volume-averaged stress is defined for the whole simulation box as

$$\sigma_{ij} = \frac{1}{V_{\text{box}}} \left[\sum_k^N (m^k v_i^k v_j^k) + \sum_k^N (r_i^k f_j^k) \right] \quad (3)$$

where $i, j = 1, 2, 3$ corresponding to the x, y, z directions and k is the identifier of an atom in the ensemble containing N atoms in a simulation box of volume V_{box} . The components of velocity and position vector for atom k are v_i^k and r_i^k respectively, while f_j^k is the force on the atom of mass m^k resulting from pairwise interaction. Since isothermal condition is applied to the system with a temperature of 0.1 K, the temperature contribution to the average stress is considered negligible.

2.3. Applied strain rates and simulation box size in MD simulations

A common challenge with MD simulations is the high strain-rates encumbered due to time-step limitations with symplectic time integration schemes, e.g. the Verlet integrator. In practice, the applied strain-rate can be orders of magnitude smaller than the maximum slip-rate, which can reach high values corresponding to dislocation velocities approaching the speed of sound. However in MD simulations, small time-scales can result in applied strain-rates that are comparable to the maximum slip-rates. Various studies have investigated the effect of strain-rates on the material response (Warner et al., 2007; Horstemeyer et al., 2001). The class of problems considered in this study deals with crack evolution, for which the strain-rate effects may influence both the thermal activation process and the stress–strain response.

In considering the thermal activation process, higher applied strain-rates allow shorter time for the system to explore alternative paths for crossing the energy barrier between two quasi-equilibrium stress states. This lowers the probability of thermal activation. A higher strain-rate results in a higher stress due to lack of thermal activation process. Therefore, the MD model developed in this work is suited for investigating deformation processes, which are mainly stress driven, as well as strain-rate effects on the mechanical response in situations which lack thermal activation. For high temperature cases, in which thermal activation dominates, the model may need to undergo modifications

On the other hand its effect on the stress–strain response is important. The stress increment $\Delta\sigma$ is determined by the relative magnitudes of the applied strain increment $\Delta\epsilon_{app}$ and the increment of plastic strain $\Delta\epsilon_{pl}$ due to dislocation motion, i.e.

$$\Delta\sigma = E_{eff}[\Delta\epsilon_{app} - \Delta\epsilon_{pl}] \quad (4)$$

where E_{eff} is an effective stiffness that can be obtained from MD simulations. A peak stress differential is defined as the peak stress minus the critical stress of dislocation emission, i.e. $\sigma' = \sigma_{peak} - \sigma_{crit}$. This is plotted in Fig. 2(a), where higher applied strain-rates are found to lead to higher stress increments. With decreasing applied strain-rates, the stress–strain response tends toward a stabilized quasi-static response. σ' is 0 for quasi-static response and monotonically increases with higher strain-rate. A higher σ' value corresponds to a departure from lower strain-rate regimes. The material properties of interest in this study are generally for strain-rates lower than 10^6 s^{-1} in Fig. 2(b). For these rates, σ' is expected to be sufficiently small. This condition is reasonably satisfied for applied strain-rates $\leq 10^8 \text{ s}^{-1}$ as shown in the Fig. 2(b).

The other important consideration in MD simulations is the simulation box size. It reflects the effect of boundary conditions and interactions. Insufficient simulation system size may lead to spurious artifacts such as image effects that should be averted to generate physically viable results. Accordingly, the simulation box size needs to be large enough such that:

- (i) crack propagation and the associated deformation mechanisms are independent of the size; and
- (ii) simulation results exhibit a monotonic convergence trend with increasing size.

In this study, MD simulations with varying simulation box sizes are examined under the conditions mentioned above. Dislocation evolution is considered to be the representative mechanism that is examined for convergence. Since the crack is assumed to go through in the z direction, dimensions in the x – y plane and in z direction are examined separately.

With respect to the x and y dimensions, the condition (i) implies that the simulation system should be large enough such that the dislocation length evolution is independent of its size, till dislocations interact with the boundary. In Fig. 3(a), the dislocation length is plotted as a function of varying system size in the x and y directions at a tensile strain of 2.4%.

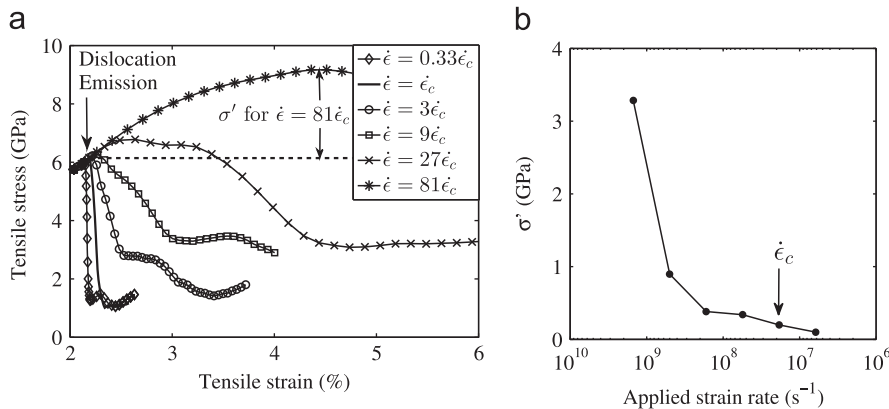


Fig. 2. (a) Tensile stress–strain response for different multiples of the applied strain-rate $\dot{\epsilon}_c \sim 2 \times 10^7 \text{ s}^{-1}$ used in Section 4 and (b) the stress change σ' as a function of the applied strain-rates with dislocation emission showing the stabilization of σ' with decreasing strain-rates.

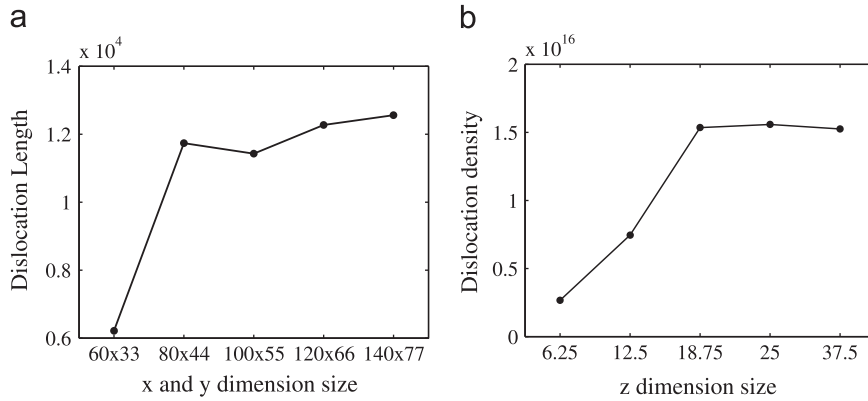


Fig. 3. Dislocation length (Å) and density (m^{-2}) for different simulation box sizes at 40 ps after dislocation nucleation, corresponding to 2.4% strain: for varying (a) x – y dimensions (nm) with fixed z dimension of 25 nm, and (b) z dimension (nm) with fixed dimensions in the x – y plane of 100 nm \times 55 nm.

Dislocations have not yet reached the boundary at this strain. The plot establishes that for sizes $\geq 80 \text{ nm} \times 44 \text{ nm} \times 25 \text{ nm}$ the total dislocation length attain similar lengths, indicating relatively insignificant boundary effect on crack tip dislocation evolution.

Dimensional sufficiency in the z direction is established with consideration of applied periodic boundary conditions, implying an infinitely extending crack. Previous atomistic studies on ductile fracture have assumed very small thicknesses $t \sim 2$ – 5 nm of the simulation box (Yamakov et al., 2006; Potirniche et al., 2006). For these cases, periodicity enforces image dislocations with distance in the z direction. The interaction between a dislocation and its image scales with thickness as: $f_{\text{image}} \propto 1/t$. For very small $t \sim O(\text{nm})$, such interactions are significantly strong that can suppress dislocation nucleation and gliding. The resulting plastic deformation is over-constrained, and hardening is generally overestimated. With increasing box thickness t , the image forces and their effect on suppression of plastic deformation decreases. The condition (ii) requires convergent trends in plastic deformation with increasing thickness. This size-effect is examined in Fig. 3(b) by plotting dislocation density evolution for different values of the z dimension. The total dislocation-length scales with the thickness, and therefore dislocation density is deemed to be a suitable variable to make the comparison. As seen in the plot, dislocation densities are much lower for smaller size systems ($l_z \leq 12.5 \text{ nm}$), which attests to the effect of suppression. For larger z dimensions ($l_z \geq 18.75 \text{ nm}$) a convergent trend is evident in the evolution of dislocation density, inferring the gradual decline in image effects. Simulation box thicknesses larger than 20 nm are considered to be appropriate. In summary, a MD simulation box with dimensions 100 nm \times 55 nm \times 25 nm is considered to adequately represent the plastic deformation process near a crack tip and is used for simulations henceforth. The upper limit of the simulation size is mainly due to the limitations of high computational resources.

2.4. The MD simulation process

Molecular dynamics (MD) simulations are carried out by efficiently by the parallel Large-scale Atomic/Molecular Massively Parallel Simulator or LAMMPS (Plimpton, 1995). In LAMMPS, the leapfrog Verlet time integration algorithm is used for integrating the Newton's equations of motion.

2.4.1. Generation of initial configurations and system equilibration

The simulation system is set up by creating atoms conforming to the atomic lattice structure and orientation of the nickel single crystal. The micro-crack at the center of the simulation box is realized by removing 3 layers of atoms such that atoms on both sides of the crack face have reduced interaction. The atom placement is followed by an energy minimization process to optimize the size in each direction, corresponding to zero barometric pressure. After the static equilibration process, atomic velocities are randomly assigned by a Maxwell–Boltzmann distribution corresponding to a system temperature of 0.1 K. Subsequently, a dynamic relaxation with a canonical NPT thermostat is applied for 10 ps at 0 Pa pressure and 0.1 K temperature to ensure the stability.

2.4.2. System simulation

At the completion of static and dynamic equilibration, uniaxial tension loading is applied in the y direction, perpendicular to crack surface at constant strain-rate of $2 \times 10^7 \text{ s}^{-1}$. A low temperature is chosen for the system, to focus on stress-driven events rather than thermally activated events. The small computational time-scale with the MD method may not be sufficient to trigger events due to thermal fluctuation. The pressure and temperature are maintained by using Nose–Hoover thermostat in the loading stage. In the MD simulations, strain is defined as the boundary displacement divided by the initial system dimension in the appropriate direction. The dislocation density, volume-fraction of twins, crack-length and crack-opening are measured in the post-processing stage by methods discussed in next the section.

Damping is introduced to suppress elastic wave reflection. The averaged stresses and energy are calculated over 100 time-steps to reduce fluctuations.

3. Characterization and quantification of deformation mechanisms

Crack propagation in face-centered cubic (fcc) crystals involves interaction with a variety of deformation mechanisms at the crack tip such as full and partial dislocations, stacking faults and twinning. A physics-based crack evolution model will be governed by quantitative measures of nucleation, evolution and interaction of these deformation mechanisms, as well as geometrical features of the crack surface. Consequently, the major objectives of the MD simulations are:

- to adequately represent deformation mechanisms near the crack tip accounting for evolution of plasticity, for a range of crystal lattice and crack orientations with respect to the loading directions;
- to qualitatively and quantitatively investigate the relation between atomic and crack configurations, and evolving deformation mechanisms;
- to quantitatively characterize evolving deformation mechanisms and crack growth and examine their effect on the material stress-strain behavior in the neighborhood of the crack.

A suite of identification and quantification methods for each mechanism is developed in this study to systematically pursue the above objectives. A summary of different mechanisms and identification methods is presented in Table 2.

Plastic deformation and damage mechanisms in metallic materials are associated with certain type of defect structures in the crystalline lattice. Investigation of the mechanisms is thus based on identification and quantitative characterization of the corresponding defect structure. It is of interest to extract the defect structure through discrete atomic information, mainly in the form of coordination and potential energy of each atom from the MD simulation results (Ackland and Jones, 2006; Kelchner et al., 1998). In nickel, full and partial dislocation cores and stacking faults are involved with atoms that no longer follow the local fcc stacking order. These dislocation cores are identified by checking the local lattice structure of the neighbors for each atom. Twinning is a volumetric defect, in which crystal lattices are rotated about the twin axes, adding symmetry through reflection across twin planes. The lattice rotation can be characterized through a deformation gradient tensor. The crack surface for this configuration may be characterized as a planar defect, in which the surface atoms have only about half the number of nearest neighbor atoms, and also have a higher potential energy. These properties may be used for differentiating crack-face atoms from others in the ensemble. Utilizing these features relevant to each defect structure, four effective methods are implemented to identify and quantitatively characterize mechanisms in the vicinity of a crack tip in the crystalline nickel lattice system as summarized in Table 2.

3.1. Common neighbor analysis (CNA)

Common neighbor analysis (CNA), proposed in Honeycutt and Anderson (1987), is used to identify the crystal lattice structure type such as fcc, bcc (body centered cubic), hcp (hexagonal close-packed), etc. The CNA algorithm is based on a nearest-neighbor map that describes the connectivity among neighbors of a central atom. A cutoff radius is used to delineate pairs of atoms that may be considered as nearest neighbors. For an atom i and its nearest neighbor atoms $j = 1, 2, \dots, n$, there exist atoms $k = 1, 2, \dots, m$, which are the common nearest neighbors of both atoms i and j . By checking the characteristics of the configuration of these common-neighbor atoms, the algorithm classifies the atom i as belonging to a lattice structure type, e.g. fcc, hcp, bcc, icosahedron etc. A local disordered atom, not belonging to any of these characteristic structures is classified as unknown. An unknown type atom normally corresponds to defects such as material surface or dislocation cores. The CNA algorithm is accurate when first and second nearest-neighbor groups are separated by distinctly different cutting radii. In the present paper, atoms at defects sites such as dislocation cores and crack surfaces are identified as “unknown”, whereas atoms at stacking faults are identified as “hcp”. Fig. 4(a) shows dislocation network near crack tip analyzed by CNA. In this analysis, dislocation cores, crack surfaces and stacking faults between two Shockley partials are identified.

CNA characterization is generally sensitive to the deformed or current configuration of atoms in the ensemble, in accurately identifying the defect structure with the exception of twinned atoms. The latter structure requires the initial configuration as reference. A major shortcoming of CNA stems from the fact that structure identification is based on

Table 2

Methods of identification and quantitative characterization of deformation mechanisms and crack geometry associated with crack propagation.

Mechanism	Dislocation	Twinning	Crack/void
Descriptor	Core structure	Lattice rotation	Nearest neighbors
Characterization	CNA		
Method	DXA	Deformation gradient	Equivalent ellipse
Quantifying variable	Total length		Crack length
	Total density	Volume fraction	Crack opening

individual atoms. It does not have the ability to provide topological structure of linear or planar defects and thus cannot delineate Burgers vectors. To investigate dislocations in more detail, atoms belonging to the dislocation cores should be connected to build the dislocation segment structure. This provides a motivation for incorporating the dislocation extraction algorithm or DXA, discussed next.

3.2. Dislocation extraction algorithm (DXA)

The dislocation extraction algorithm or DXA developed in Stukowski and Albe (2010), is a powerful method to characterize the topological structure of dislocations in a crystalline material. It assembles atoms at dislocation cores that are identified by CNA, based on topological connectivity to construct dislocation segments, and also to find the Burgers vector associated with each segment. Instead of providing the local structure information for each atom, DXA assumes a dislocation segment to be the analysis unit. For each segment, the dislocation length and Burgers vector are calculated. This makes calculating the dislocation density, as well as analyzing the dislocation reaction convenient. Since the first step of DXA is finding the dislocation core atoms by CNA, reliability of the CNA is a necessary prerequisite for DXA. A comparison of the outputs of the CNA and DXA are shown in Fig. 4, in which the dislocation line structure by DXA is compared with a MD simulation snapshot colored by CNA. The atomic configuration in Fig. 4(a) is transformed to the dislocation line structure in Fig. 4(b).

3.3. Atomic-scale deformation gradient

In continuum mechanics, the deformation gradient $\mathbf{F} = \partial \mathbf{x} / \partial \mathbf{X}$ is a second-order tensor that provides a robust measure of material deformation, including shape change and overall material rotation. It is desirable to develop such a robust metric for estimating the deformation gradient tensor in atomic configurations to delineate the stretch and rotation of the local lattice structure. While, it is not possible to replicate this exact measure for the discrete topologies in MD simulations, a least-square minimization-based methodology has been proposed in Zimmerman et al. (2009) for estimating the deformation gradient \mathbf{F} in atomic lattices. For a given atomic location x^α and its n nearest-neighbors in the deformed atomic configuration, a least-square regression analysis solves for a “local-averaged” deformation gradient tensor \mathbf{F}^α by minimizing each component i of a residual vector B_i^α , defined as

$$B_i^\alpha = \sum_{\beta=1}^n (x_i^{\alpha\beta} - F_{ij}^\alpha X_j^{\alpha\beta})^2 \quad (5)$$

where $x^{\alpha\beta}$ is an inter-atomic separation vector in the deformed configuration for the α – β near-neighbor pair, and $X^{\alpha\beta}$ is the corresponding vector in the reference configuration, for each atom α . Components of \mathbf{F} in the regression equation are

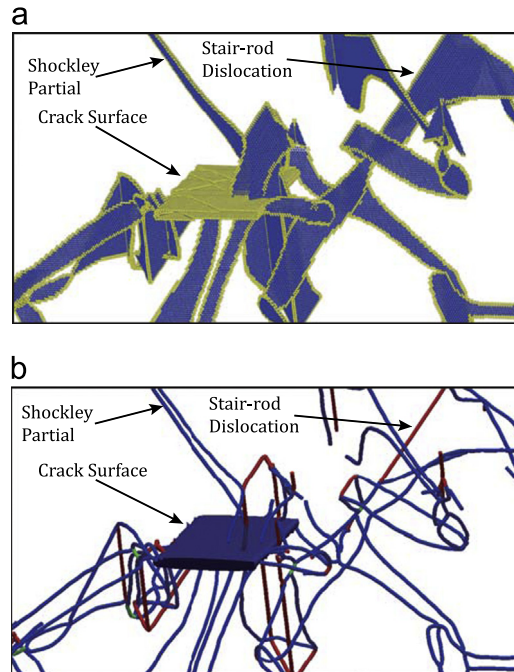


Fig. 4. Dislocation network evolution near the crack, characterized by both CNA and DXA; (a) all non-fcc atoms are delineated by CNA: (red atoms are at dislocation cores or crack surface, blue atoms are at stacking faults); (b) dislocation segments extracted by DXA, colored by the magnitude of Burgers vector (blue lines represent Shockley partials, red and green lines represent stair-rod dislocations). (For interpretation of the references to color in this figure caption, the reader is referred to the web version of this article.)

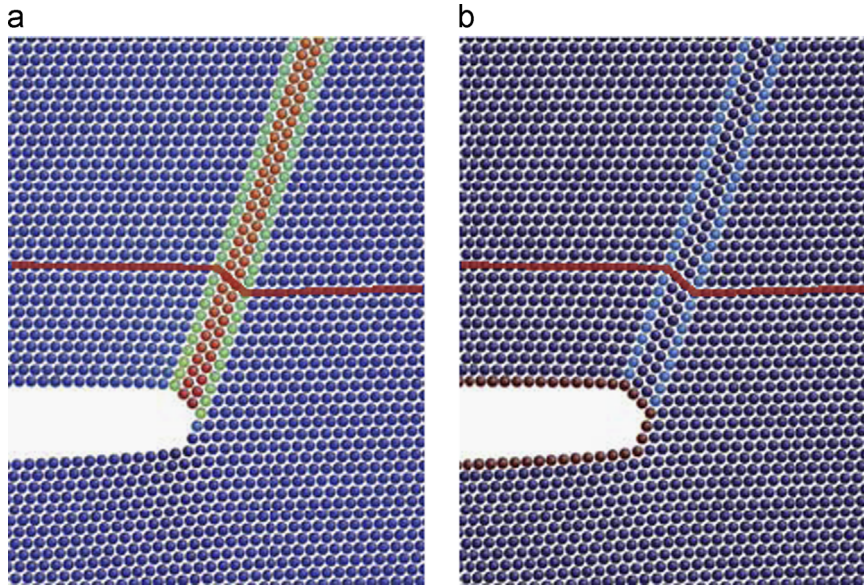


Fig. 5. A two-layer micro-twin nucleated at the crack tip in MD simulations, colored by different methods: (a) colored by one component of the local deformation gradient \mathbf{F}_{21} (red corresponds to twinned region, green is the twin boundary and blue is the parent region); (b) colored by CNA (only twin boundary is identified but not the twinned region). The twinned region is rotated by 38.94° . (For interpretation of the references to color in this figure caption, the reader is referred to the web version of this article.)

Table 3

Comparison of measured values of deformation gradient components for atoms inside the twin, with reference values obtained for pure rotation without any applied strain or thermal fluctuation.

F Component	Measured value			Reference pure rotation value
\mathbf{F}_{11}	0.767	0.767	0.766	0.778
\mathbf{F}_{12}	−0.0768	−0.0766	−0.0780	−0.0785
\mathbf{F}_{21}	0.651	0.652	0.653	0.628
\mathbf{F}_{22}	1.276	1.273	1.275	1.222

obtained by minimizing B_i^α , i.e. by enforcing the relation:

$$\partial B_i^\alpha / \partial F_{iM}^\alpha = 0 \quad \forall i, M \quad (6)$$

Correspondingly the atomic-scale deformation gradient tensor is expressed as

$$F_{ij}^\alpha = \omega_{iM}^\alpha (\eta^\alpha)^{-1}_{MJ} \quad \text{where} \quad (7a)$$

$$\omega_{iM}^\alpha = \sum_{\beta=1}^n (X^{\alpha\beta})_i (X^{\alpha\beta})_M \quad \text{and} \quad \eta_{MJ}^\alpha = \sum_{\beta=1}^n (X^{\alpha\beta})_M (X^{\alpha\beta})_J \quad (7b)$$

The deformation gradient can identify twinned regions in the fcc structure. For example, Fig. 5 shows a comparison of the a crack-tip nucleated micro-twin, identified by the deformation gradient and CNA methods respectively. The configuration has been subjected to a 5% tensile strain in the y direction. This results in a 1.5% compressive strain in the x direction due to the Poisson effect. The twin boundary is a $\Sigma 3$ grain boundary with 38.94° tile angle. The non-twinned, twinned and twin boundary regions are clearly separated by the deformation gradient value in Fig. 5(a). On the other hand, the CNA is only able to identify the twin boundaries in Fig. 5(b). The components of the \mathbf{F} tensor in the x – y plane are shown in Table 3. The reference value inside the twin corresponds to a pure rotation of the atomic lattice without any applied strain or thermal vibration, i.e. $\mathbf{F} = \mathbf{R}$. The three sets of measured values (in the three columns) are evaluated by randomly choosing the atom α inside the twinned region for deformation gradient analysis using (7). The measured components of \mathbf{F} for the three atoms shows concurrence. The difference between the deformed and reference values of \mathbf{F}_{22} is $\sim 5\%$, while that for \mathbf{F}_{11} is $\sim 1.5\%$. This is due to the effect of applied strain in the measured values.

3.4. Crack configuration (length and opening)

Crack propagation in the atomic lattices can commence in multiple modes, e.g. brittle mode due to cleavage, ductile mode with void nucleation, growth and coalescence, or a combination of the two. It is important to parameterize the

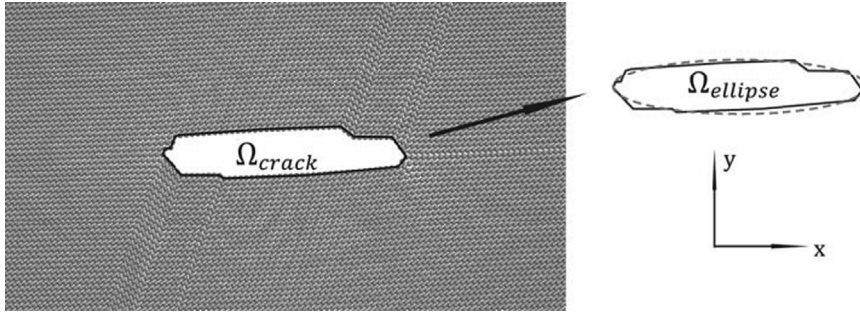


Fig. 6. The crack geometry is characterized by the dimension of the major/minor axis of the ellipse.

geometric features of the crack to characterize the crack modes, as well as quantify its evolution. The parameters can be used in a continuum level constitutive model for the crack. In this paper, the crack geometry and its evolution in the x – y –plane is of primary interest, since the crack has translation symmetry in the z direction. To parameterize an irregular crack surface in the MD simulations, an equivalent ellipse is introduced as the approximation to the crack geometry in the x – y –plane as shown in Fig. 6. The equivalent ellipse is defined by five parameters, viz. (i) x_c, y_c centroidal coordinates (x_c, y_c), (ii) the major and minor axes (a, b), and (iii) the orientation angle (θ) of the major axis of the equivalent ellipse. The major and minor axes represent the length and opening of the crack respectively. This parameterization helps in monitoring the evolution of the crack length and crack opening from MD simulation.

Generation of the equivalent ellipse is achieved by equating the zero-th, first and second geometric moments of inertia of the ellipse to moments of the irregular crack profile in the molecular structure. The latter is obtained by setting up a fine square grid to completely contain the crack opening. Equations representing moment equivalence are

$$\begin{aligned}
 (a) \quad I_0 &= \iint_{\Omega_c} dx dy = \sum_{I=1}^{NUSG} A_I \\
 (b) \quad I_x &= \iint_{\Omega_c} x dx dy = \sum_{I=1}^{NUSG} x_I A_I, \quad I_y = \iint_{\Omega_c} y dx dy = \sum_{I=1}^{NUSG} y_I A_I \\
 (c) \quad I_{xx} &= \iint_{\Omega_c} x^2 dx dy = \sum_{I=1}^{NUSG} x_I^2 A_I, \quad I_{yy} = \iint_{\Omega_c} y^2 dx dy = \sum_{I=1}^{NUSG} y_I^2 A_I \\
 I_{xy} &= \iint_{\Omega_c} xy dx dy = \sum_{I=1}^{NUSG} x_I y_I A_I
 \end{aligned} \tag{8}$$

where x_I, y_I, A_I correspond to the centroidal coordinates and area of the I -th square-grid in the molecular image and $NUSG$ is the total number of squares in the grid. The centroid (x_c, y_c), major and minor axes (a, b), and angular orientation θ of the major axis are then obtained in the following sequence:

- First, the centroidal coordinates are evaluated using the equations:

$$x_c = \frac{I_x}{I_0}, \quad y_c = \frac{I_y}{I_0} \tag{9}$$

- Next, the second moments are written in terms of coordinates with origin at x_c, y_c as $I_{xx}^c, I_{yy}^c, I_{xy}^c$. The ellipse orientation θ corresponds to that for which the rotated $I_{xy}^c = 0$, where the superscript c corresponds to a centroidal coordinate system that is oriented along the principal axes of the ellipse. The major axis orientation is given as

$$\theta = \frac{1}{2} \tan^{-1} \left(\frac{-2I_{xy}^c}{I_{xx}^c - I_{yy}^c} \right) \tag{10}$$

- Finally, the lengths of the major and minor axes are calculated from moments in the rotated coordinate system as

$$b = \left(\frac{4I_{xx}^c}{I_0} \right)^{1/2} \quad \text{and} \quad a = \frac{I_0}{\pi b} \tag{11}$$

4. MD simulation results for different lattice orientations

MD simulations are conducted for three different lattice orientations, following the discussions in Section 2. The orientations correspond to the following directions for the x – y – z axes in Fig. 1(a):

1. Lattice Orientation 1: $x \rightarrow [\bar{1}10]$, $y \rightarrow [111]$, $z \rightarrow [11\bar{2}]$
2. Lattice Orientation 2: $x \rightarrow [11\bar{2}]$, $y \rightarrow [111]$, $z \rightarrow [\bar{1}\bar{1}0]$
3. Lattice Orientation 3: $x \rightarrow [100]$, $y \rightarrow [010]$, $z \rightarrow [001]$

These simulations investigate the atomic-level crack propagation and associated deformation mechanisms, along with the overall stress–strain response of the ensemble. Deformation mechanisms, such as dislocations and twinning are important in relating the state of the molecular system to its overall behavior, subject to different loads. This section explores the effect of lattice orientation and crack tip geometry on the activation and evolution of different deformation mechanisms. As discussed earlier, this work focuses on stress-driven phenomena, where thermal fluctuation contributes negligible energy for system crossing energy barrier.

4.1. Lattice orientation 1

For the lattice orientation 1, there are 3 slip planes viz. $(\bar{1}\bar{1}1)$, $(\bar{1}\bar{1}\bar{1})$ and $(11\bar{1})$ that have the same largest in-plane stress, while the (111) plane has zero in-plane stress. Fig. 7 depicts the evolution of deformation mechanisms near the crack surface. The load is applied on the simulation box in the form of a constant, tensile engineering strain-rate. Under this load, the system first undergoes elastic deformation. After reaching a critical stress of ~ 5.6 GPa, partial dislocation emission is observed from the crack tip in both the $(\bar{1}\bar{1}1)$ and $(\bar{1}\bar{1}\bar{1})$ planes, as shown in Fig. 7(a). Subsequent to dislocation nucleation, slip caused by dislocation gliding in these planes blunts the crack tip and reduces stress concentration. No brittle crack propagation by atomic bond cleavage is observed for this simulation. Crack evolution for this orientation is mainly governed

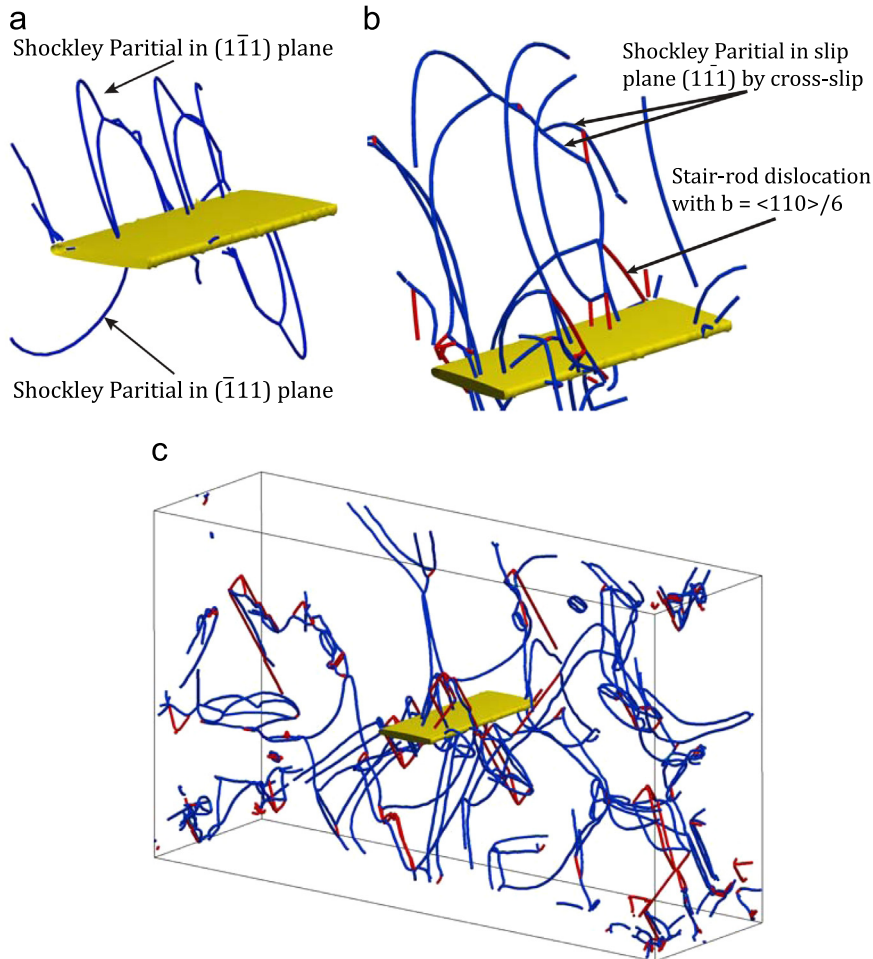


Fig. 7. Snapshots of deformation mechanisms in the presence of the crack, with only the crack surface and dislocations visible; (a) dislocations in 2 slip planes nucleated from the crack tip after reaching critical stress; (b) cross-slip and formation of stair-rod dislocations; and (c) stabilized dislocation structure at about 2.7% strain. The dislocation segments are colored by the magnitude of their Burgers vectors, viz. blue, red and green correspond to $b^2 = \frac{1}{18}a^2$, $\frac{1}{9}a^2$, $\frac{1}{6}a^2$ respectively, while the crack surface is in yellow (For interpretation of the references to color in this figure caption, the reader is referred to the web version of this article.).

by the hydrostatic strain and crystallographic slip, resembling the void growth process. This is consistent with experimental observations (Patil et al., 2009) that trans-granular cracks in nickel under mode-I loading experience significant crack-tip plasticity resulting in crack blunting. Consequently, this study focuses on investigating the plastic deformation process near the crack tip. It is observed that besides dislocation gliding on the slip planes, cross-slip and formation of dislocation junctions are also important mechanisms. Cross-slip require the formation of full screw dislocation and enables dislocation gliding from the original slip plane onto other slip planes. In Fig. 7(b), it is seen that there exists dislocation gliding in the $(11\bar{1})$ plane as the result of cross-slip. When two partial dislocations on different slip planes meet, they can form stair-rod dislocation (Thompson, 1954; Hirth and Lothe, 1982). The dislocation line is always along the line of intersection of the corresponding two slip planes, i.e. along $[110]$ type directions. Extensive studies in Hirth and Lothe (1982) have proposed four types of reaction formation, of which, two are observed in the present simulations, viz.

$$\frac{1}{6}\langle 2\bar{1}\bar{1} \rangle + \frac{1}{6}\langle \bar{1}21 \rangle \rightarrow \frac{1}{6}\langle 110 \rangle \quad (12a)$$

$$\frac{1}{6}\langle 12\bar{1} \rangle + \frac{1}{6}\langle 12\bar{1} \rangle \rightarrow \frac{1}{3}\langle 100 \rangle \quad (12b)$$

Fig. 7(b) shows the stair-rod dislocation (colored red and green) connecting stacking faults in two slip planes, where the red line segments correspond to $\frac{1}{6}\langle 110 \rangle$ type, as a result of the first reaction. A simple analysis shows that stair-rod dislocations do not belong to any slip system in either glide plane, and they are generally resistant to glide or climb. The formation of stair-rod dislocations provides obstacles to the motion of other dislocations. It is therefore directly related to the flow stress and hardening behavior. In the simulation, the total length of stair-rod dislocation is about 40% of the total dislocation length. Such high content of sessile dislocations limits the length of mobile dislocation segments, which results in very high flow stresses at the crack tip. Fig. 7(c) shows the dislocation structure after they have stabilized, in the sense that most of them have stopped gliding.

The volume-averaged tensile stress in the y - direction, dislocation density and crack surface parameter evolution as a function of the increasing applied strain plotted in Fig. 8. In the tensile stress–strain curve, the peak stress corresponds to the critical resolved shear stress required for nucleating the dislocation. The stress subsequently decreases due to the motion of dislocation, which releases the elastic strain in the system. The figure shows that the softening is followed by a hardening stage, where the flow stress is governed by the dislocation structure.

4.2. Lattice orientation 2

While for this lattice orientation, a loading direction along $[111]$ yields the same Schmid factor for all slip systems as lattice orientation 1, different deformation mechanisms are observed due to the crack geometry. Deformation mechanisms in this orientation can be divided into two main categories, viz. (i) only twin partials contributing to slip, and (ii) dislocation motion contributing to slip. The tensile stress, dislocation density, twin volume fraction and crack geometry evolution as a function of increasing applied strain are shown in Fig. 9. The system first undergoes elastic deformation until $\sim 1.6\%$ strain, at which micro-twins are nucleated. These are subsequently coarsened by twin partial dislocation emission in adjacent slip planes (in this case the $\{11\bar{1}\}$ plane). The crack-front is along the $[1\bar{1}0]$ direction, which is parallel to the emitted leading partial dislocation line. The existence of the twinning mode suggests that this specific geometry suppresses the trailing partial emission. Consequently, the likelihood of leading partials being nucleated in adjacent plane increases. The correlation between twin formation and $[1\bar{1}0]$ being an translation symmetry direction has also been observed in previous MD simulations, e.g. Yamakov et al. (2002) and Tadmor and Hai (2003). In the twin dominated stage as shown in Fig. 9(a), the density of twin partial dislocations is an order of magnitude smaller than that in lattice orientation 1, where deformation is dominated by the nucleation of dislocation loops. This corroborates that twins have much less ability of carrying plastic flow than dislocations. At about $\sim 3.3\%$ tensile strain, a dislocation loop starts to emit from the crack tip, gliding in the $\{1\bar{1}1\}$ plane. With more dislocation nucleation in different slip planes, the average tensile stress in the MD system decreases significantly. This slip-rate surge stage is similar to the lattice orientation 1, since dislocation motion becomes the major deformation mechanism.

The twin boundary-dislocation interaction is important in the presence of both twins and dislocations. Twin boundaries act as obstacles to the motion of dislocations. A critical shear stress is needed for the dislocations to penetrate twin boundaries into the twinned region. When dislocations glide on a slip plane and stop at a twin boundary, the dislocation line becomes parallel to the line of intersection of the slip plane and the twin boundary plane, as shown in Fig. 10. With sufficient shear stress, dislocations interact with the twin boundary in complicated way depending on the incoming dislocation and the local stress state (Zhu et al., 2011). This results in mechanisms of dislocation dissociation with the formation of stair-rod dislocations, and dislocation transmission across twin boundaries as well as cross-slip. These mechanisms dominate the flow stress evolution for applied strains larger than 3.8%. The effects are shown in the stress–strain curve of Fig. 9(a), which is found to be oscillatory in this range.

In summary, the simulations suggest that nucleation of micro-twin band at the crack tip occurs for a specific crack geometry and lattice orientation. The deformation twin has very limited ability of contributing to slip without the

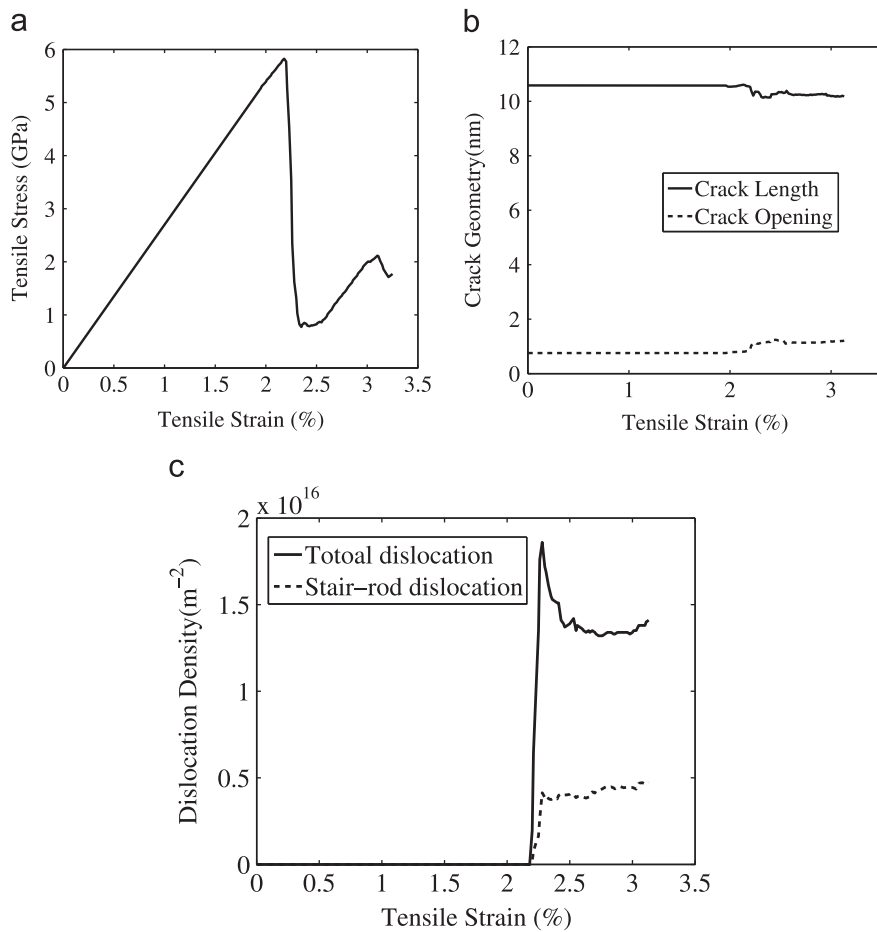


Fig. 8. Evolution of variables for lattice orientation 1: (a) averaged tensile stress, (b) crack length and opening evolution, and (c) density of stair-rod dislocations and total dislocation density, as a function of increasing applied strain.

nucleation of a dislocation loop. The major role of twinning in plastic deformation of Nickel is to put up obstacles to dislocation gliding with complex interactions. These mechanisms control the flow stress in twinned microstructures.

4.3. Lattice orientation 3

In this lattice orientation 3, all four (111) slip planes are activated and share the same in-plane stress. At $\sim 5.2\%$ tensile strain, the crack propagates slightly by forming an amorphous zone near the tip. This is followed by partial dislocation emission in all four (111) planes, as shown in Fig. 11(a). Similar to the lattice orientation 1 deformation, the dislocation activity causes crack-tip blunting and inhibits further crack propagation. Significant amount of stair-rod dislocation formation by slip system interaction is also found as seen in Fig. 11(b), which depicts a stabilized dislocation structure. In this configuration, the length of stair-rod dislocation takes is about 40% of total dislocation length.

The tensile stress, dislocation density and crack surface dimension evolution as a function of the applied strain is shown in Fig. 12. The stress-strain behavior in Fig. 12(a) exhibits three stages similar to lattice orientation 1. The first is the elastic deformation stage, followed by a slip-rate surge stage during which most dislocations are mobile and gliding fast in their slip planes. The final is the hardening stage during which the tensile flow stress is governed by dislocation structures, especially dislocation junctions which serve as pinned points and obstacles to the motion of other dislocations. Due to additional slip planes activated, the system contains larger dislocation density in comparison with lattice orientation 1.

5. Studies involving energy partitioning in the molecular system

A comprehensive understanding of ductile fracture requires a delineation of the energy contribution from different deformation mechanisms. The dissipated energy, associated with inelastic mechanisms, dominates crack evolution. Partitioning of the energy in MD simulations, based on quantification of mechanisms, may be used effectively to understand the thermodynamic process at the crack tip. This in turn can help in developing governing equations for crack propagation

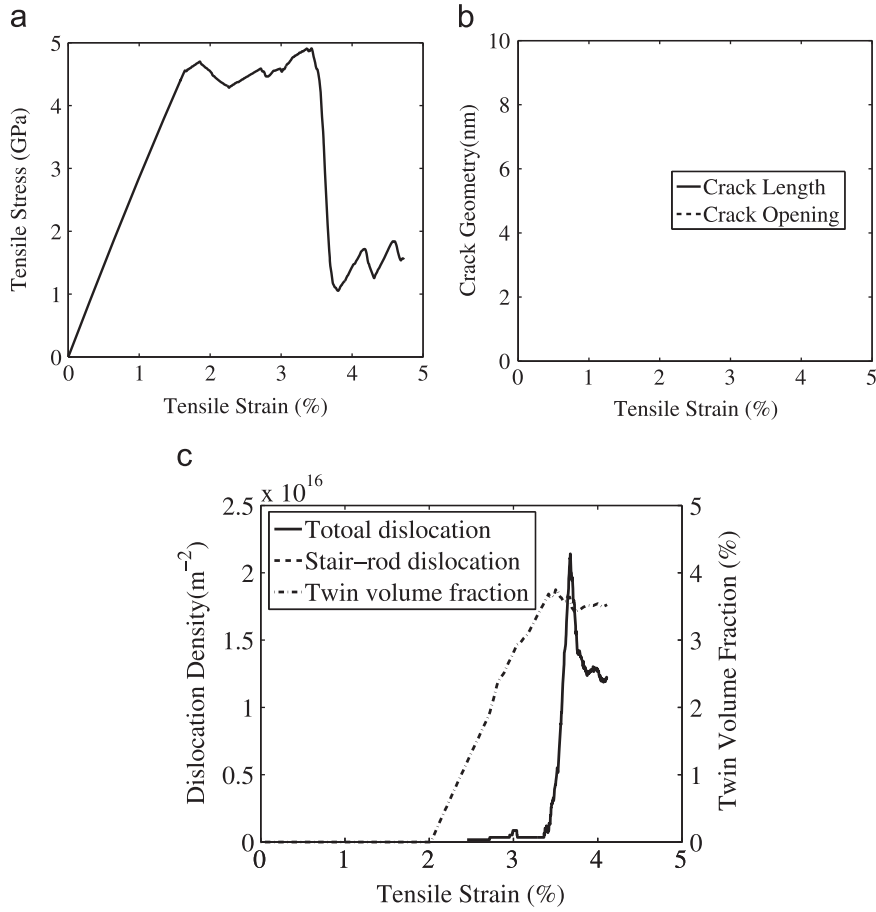


Fig. 9. Evolution of variables for lattice orientation 2: (a) averaged tensile stress, (b) crack length and opening evolution, and (c) density of stair-rod dislocations, total dislocation density and twin volume fraction, as a function of increasing applied strain.

and associated near-field deformation. The incremental energy near a crack in the MD domain is assumed to be decomposed into the following components:

$$dW = dQ + dU_{el} + dU_{inel} + 2\gamma_s dA = dQ + dU \quad (13)$$

dW is the increment of work done due to the applied loading, dQ is the generated heat, dU_{el} is the incremental elastic energy that is recovered by unloading, and dU_{inel} is the strain energy increment associated with deformation mechanisms and defects such as dislocations, twin boundaries and stacking faults. The term $2\gamma_s dA$ corresponds to the surface energy caused by the formation of crack surfaces, where γ_s is the surface energy and dA is the increment of crack surface area. The total strain energy increment dU is divided into the recoverable elastic, irrecoverable inelastic and surface energy increments. Different energy components in Eq. (13) are evaluated using the following steps.

The work increment is calculated as $dW = P A_{xz} dy$, where P , A_{xz} , dy are the applied pressure, surface area and displacement on xz -plane respectively. dU corresponds to the total potential energy of the MD system, which is evaluated from MD simulations, based on the inter-atomic potential and coordination of each atom. The heat generated is calculated from the relation $dQ = dW - dU$. The elastic energy dU_{el} is obtained by unloading the system and evaluating the energy difference in the molecular system, i.e. $dU_{el} = dU - dU_{unload}$. The sum $dU_{inel} + dQ$ corresponds to the total dissipation due to plastic deformation. For the two-dimensional propagation simulated by MD in this work, the crack surface increment is $dA = l_z \cdot da$, where l_z is the thickness and da is the change in crack length. The latter is calculated from the equivalent ellipse approach in Section 3.4 using the second of equation (11). With dU , dU_{el} and $2\gamma_s dA$ known, the increment of strain energy associated with defects is assessed as $dU_{inel} = dU - dU_{el} - 2\gamma_s dA$. In the MD simulations considered for the three lattice orientations, crack propagation is negligible compared with other terms and hence the surface energy contribution is ignored.

In Figs. 13–15, the evolution of U_{el} , U_{inel} and $U_{inel} + Q$ are plotted as a function of increasing applied strain. Specifically, the figures show the correlation between the inelastic strain energy and quantification of defects for three lattice orientations. In Figs. 13 and 15 U_{inel} is correlated to the dislocation density ρ_{dis} , whereas in Fig. 14 it is correlated to ρ_{dis} and the twin volume fraction. Both the dislocation density and twin volume fraction are normalized with respect to the maximum values

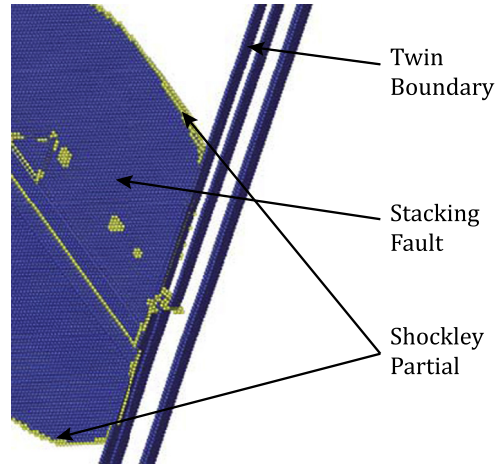


Fig. 10. Snapshot at $\sim 3.5\%$ strain, showing the dislocation-twin interaction due to part of the partial dislocation loop blocked by the twin boundary. Atoms are colored by the CNA value: yellow denotes atoms at the dislocation cores or surfaces, and blue denotes atoms in the stacking faults or twin boundaries (For interpretation of the references to color in this figure caption, the reader is referred to the web version of this article.).

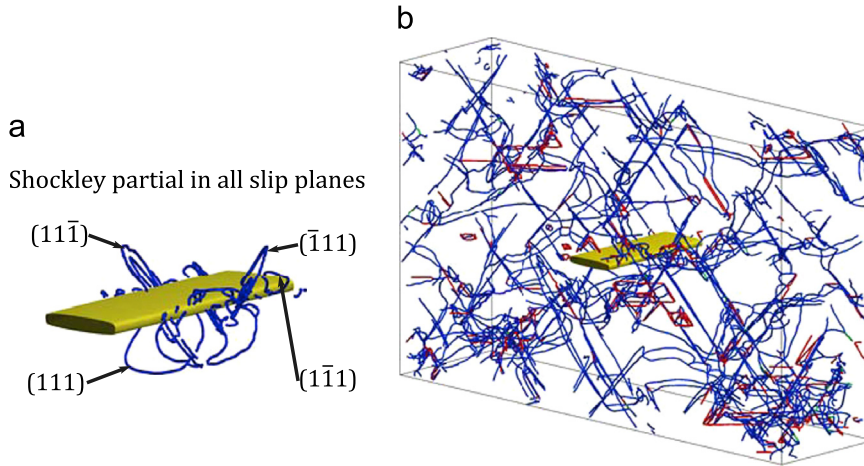


Fig. 11. Snapshots of deformation mechanisms for lattice orientation 3 with only crack surface and dislocations visible: (a) zoomed in region of the dislocations first nucleated from the crack-tip in all 4 slip planes after reaching critical stress; (b) overall stabilized dislocation structure along with the crack surface at about 6% strain (For interpretation of the references to color in this figure caption, the reader is referred to the web version of this article.).

of $\rho_{dislocation} \cdot f_{twin}$, i.e. with ρ_0, f_0 . These correlation relationships are vital in developing physics-based constitutive relations that relate inelastic dissipation to the corresponding deformation mechanisms.

An assumption made is that the total energy of the dislocation network is the sum of strain energy of individual dislocation segments. Using the following relation for energy per unit length in terms of the Burgers vector b of a dislocation segment

$$dU_{dis}/dl \propto Gb^2 \quad (14)$$

where G is the shear modulus, the total energy of dislocations can be estimated by integrating equation (14) as:

$$U_{dis} \propto \rho_{dis}^{sum} V G b^2 j \quad (15)$$

The total dislocation density is defined as the sum of contributions from Shockley partials and stair-rod dislocations, i.e. $\rho_{dis}^{sum} = \rho_{Shockley} + \rho_{stairrod}/3$, where two density terms are quantified using approaches discussed in Section 3. The value of b^2 is different for the two types of dislocations. For Shockley partial dislocation $b^2 = a^2/6$, while for stair-rod dislocation $b^2 = a^2/18$. Eq. (15) gives a direct relation between the evolution of ρ_{dis}^{sum} to the increase in dislocation energy. While this simple relation does not separately capture the effects screw and edge dislocations, nor the interaction of stress fields of adjacent dislocations, the linear correlation is still deemed to hold.

Good consistency is observed in the evolution of the dislocation energy and inelastic energy for dislocation dominated deformation in Figs. 13(b) and 15(b), corresponding to lattice orientations 1 and 3. This corroborates the postulate that the inelastic strain energy dU_{inel} obtained using the unloading process adequately represents the strain energy associated with

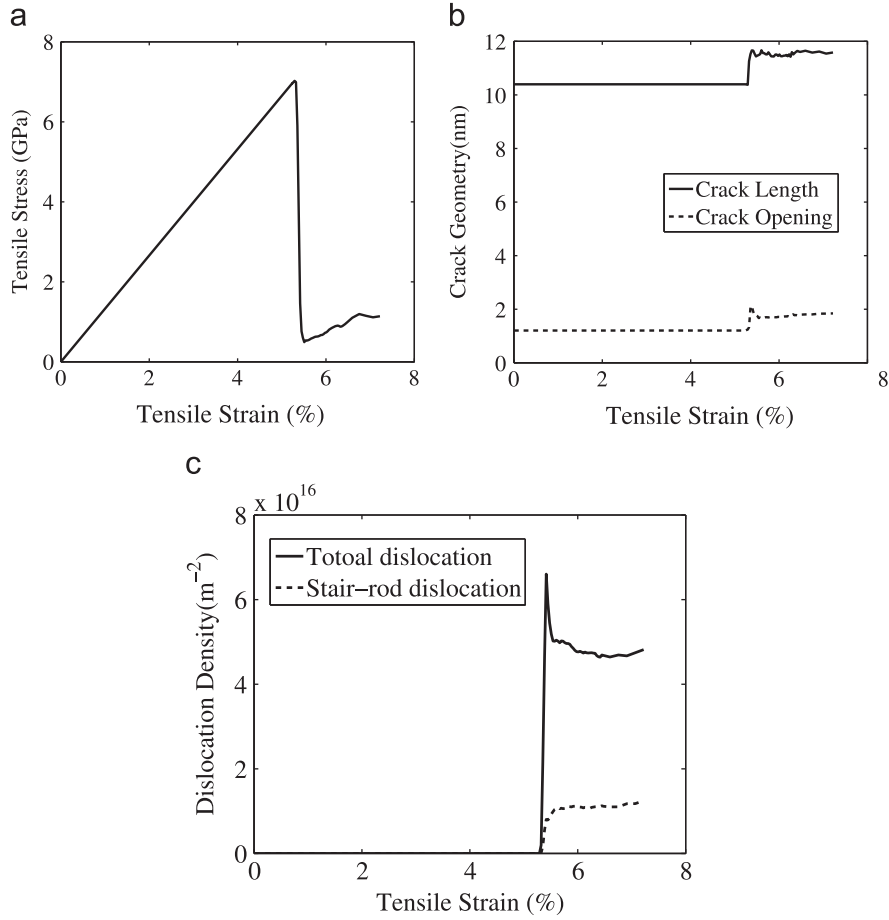


Fig. 12. Evolution of variables for lattice orientation 3: (a) averaged tensile stress, (b) crack length and opening evolution, and (c) density of stair-rod dislocations and total dislocation density, as a function of increasing applied strain.

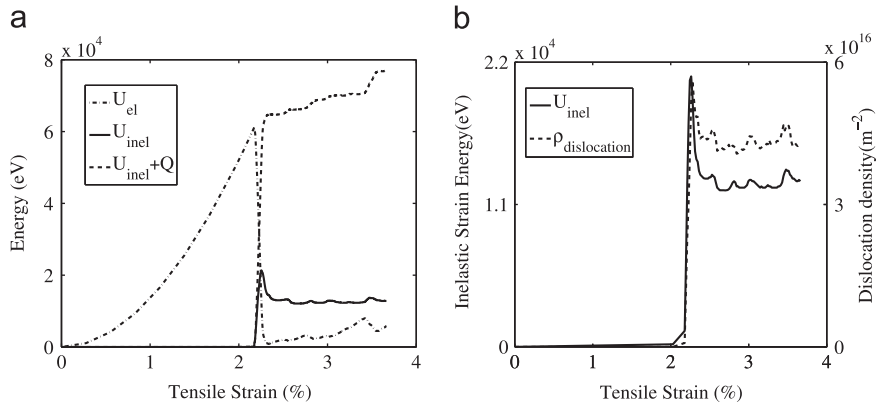


Fig. 13. For lattice orientation 1: (a) Evolution of elastic strain energy U_{el} , dissipated energy due to plastic deformation $U_{inel} + Q$ and the inelastic strain energy U_{inel} as functions of applied strain; (b) correlating the inelastic strain energy U_{inel} to the dislocation density ρ_{dis} .

the dislocation structure. The deviation from a perfectly linear correlation is justified, as the functional relation (15) does not account for the interaction of stress fields. The plot for lattice orientation 2 in Fig. 14(b) accounts for both twinning and dislocations contributing to the plastic deformation. Twins contribute more to the inelastic energy than dislocations. Furthermore, the interaction between dislocations and twins actually reduce the inelastic strain energy. It should be noted that the inelastic strain energy of dislocations are more than just the defect energy of dislocation cores. For dislocations, U_{inel} is mainly the strain energy associated with elastic field. For micro-twins with thickness of a few atomic layers, the defect energy is mainly from the twin boundary energy.

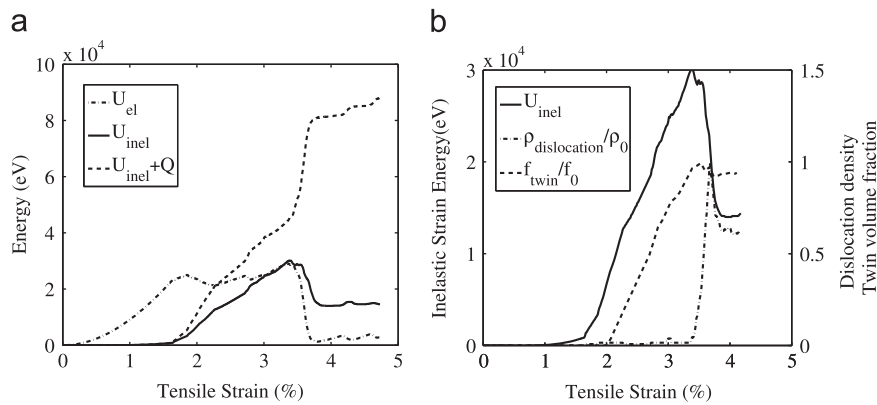


Fig. 14. For lattice orientation 2: (a) Evolution of elastic strain energy U_{el} , plastic dissipation $U_{inel} + Q$ and the inelastic strain energy U_{inel} as functions of applied strain; (b) correlating inelastic strain energy U_{inel} to the dislocation density ρ_{dis} and twin volume fraction. The dislocation density and twin volume fraction are normalized with respect to ρ_0, f_0 corresponding to the maximum values of $\rho_{dis} \cdot f_{twin}$ respectively, to be in the 0–1 range.

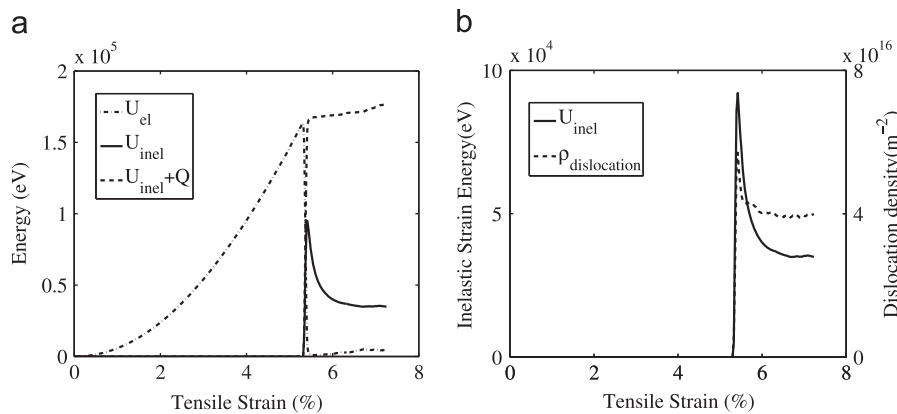


Fig. 15. For lattice orientation 3: (a) Evolution of elastic strain energy U_{el} , plastic dissipation energy $U_{inel} + Q$ and the inelastic strain energy U_{inel} as functions of applied strain; (b) correlating inelastic strain energy U_{inel} to the dislocation density ρ_{dis} .

Energy evolution during the predominantly twinning and dislocation stages of deformation in lattice orientations 2, are studied from the plot of Fig. 14(a). The ratio of the defect energy to the generated heat is quite different during these stages. The defect energy is about 60% of the total dissipation for twinning, while it is only about 20% for the dislocation dominated stage. Similar percentages of dislocation energy are also observed for lattice orientations 1 and 3. A heat conversion ratio μ is defined as the ratio of heat dissipation to the total dissipation. MD simulation results show that $\mu \approx 0.8$ for dislocation and $\mu \approx 0.4$ for twinning. This suggests that for twinning to be the dominating deformation mechanism, much lower heat conversion ratio should be used. Similar analysis can be applied to qualitatively evaluate heat conversion ratio for other deformation mechanisms.

6. A simple mechanistic model of deformation from MD simulations in the presence of a crack

Comprehension of the intrinsic relations between mechanisms and mechanical behavior, with consideration of strain-rate and size effects, is needed for the development of constitutive and crack evolution relations from atomistic simulations. Energy partitioning, based on quantification of different deformation mechanisms in the atomistic simulations, allows for the association of specific mechanisms with different components contributing to the total energy of the system. This is an important step in developing coupled constitutive-crack models. In Section 5, the discussions have shown that the atomistic model for Nickel does not exhibit any appreciable crack propagation for the simulation conditions considered. In contrast, the pre-existing crack causes nucleation of dislocations and other mechanisms leading to significant plastic deformation. Consequently, it is not possible to derive appropriate crack evolution laws from these simulations. However, it is possible to develop a simple mechanistic model of deformation that accounts for the deformation mechanisms in a crystalline material in the presence of a crack. Discussions in Section 4 have demonstrated that dissipative mechanisms and stress-strain relations associated with crack evolution in atomic systems have significant orientation dependence.

A simple model, connecting dislocation evolution and motion, with slip-rates is conceived for understanding the effectiveness of atomistic simulations in bridging discrete atomic to crystalline length scales. The model focuses on the

aggregate behavior, rather than nucleation or motion of a single defect, with dislocation density and averaged stresses representing the system variables. In the atomic simulations of Section 4, the lattice orientation and tensile loading direction are chosen such that all activated $\frac{1}{2}\langle 110 \rangle \langle 111 \rangle$ slip systems share the same Schmid factor m . Simple calculations show that for the lattice orientations 1 and 2, 6 active slip systems have a Schmid factor $m=0.272$, while the remaining 6 have $m=0$. For the lattice orientation 3, 8 active slip systems have $m=0.408$ while the remaining 4 slip systems have $m=0$. For an applied constant strain-rate $\dot{\epsilon}_{\infty}$ in the y -direction, the tensile stress-rate is calculated from the slip-rate using Orowan's equation as

$$\dot{\sigma}_{yy} = E_{\text{eff}}[\dot{\epsilon}_{\infty} - m\dot{\gamma}_{pl}] = E_{\text{eff}}[\dot{\epsilon}_{\infty} - m\rho_m b v] \quad (16)$$

where σ_{yy} is the y -direction tensile stress, E_{eff} is the effective stiffness which can be obtained by unloading and m is the Schmid factor associated with the activated $\frac{1}{2}\langle 110 \rangle \langle 111 \rangle$ slip system. For this system, γ_{pl} is the plastic slip, ρ_m is the mobile dislocation density, b is the Burgers vector and v is the average dislocation velocity. The mobile dislocation density is obtained as a fraction f_m of the total dislocation density ρ (both mobile and immobile) that can be obtained by DXA in Section 3.2, following the relation $\rho_m = f_m \rho$. Dislocation mobility results from a competition between the driving resolved shear stress and the resistance due to interactions of dislocations. In the present simulations, this resistance can be very strong due to two major mechanisms viz.:

1. High dislocation density of $O(10^{16}) \text{ m}^{-2}$ results in very small spacing in between the dislocations;
2. Formation of stair-rod dislocations serve as strong barrier to the dislocation motion.

Following Gilman (1969), it is assumed that f_m decays exponentially with increasing dislocation density (plastic strain) and decreasing resolved shear stress. This yields the mobile dislocation density as

$$\rho_m = K \rho e^{-(A\rho/\tau)} \quad (17)$$

where A is a constant that controls the decay rate. The coefficient K accounts for the effective dislocation length and has a value ~ 0.3 . Since total dislocation length consists of segments of predominantly Shockley partials yet the Burger vector is taken for full dislocations; also the effective length for curved dislocation segments is smaller than the actual segment length.

The averaged dislocation velocity in the Orowan's equation has been conventionally expressed as either a power law or exponential function of the applied stress (Hutchinson, 1976; Kocks et al., 1975). While good agreement with experiments at low applied stresses has been argued for the power law (Gilman and Johnston, 1962), the exponential form generally provides better approximation for a wider range of stresses. Since in the present MD simulations, the resolved shear stress is of $O(1 \text{ GPa})$ and dislocations move at approximately the shear-wave speed, the exponential form is assumed to provide a better description. Consequently the averaged dislocation velocity is expressed as

$$v = c_s e^{-\beta/\tau} \quad (18)$$

where c_s is the shear-wave velocity taken to be 3020 m/s and β is the drag force that is experimentally determined to be 475 MPa in Dimiduk et al. (2005). For $\tau \gg \beta$, the velocity converges to c_s . The use of the exponential form has also been suggested in the MD simulation studies of Olmsted et al. (2005) under a range of shear stress from 0–5 GPa. Substituting Eqs. (17) and (18) in Eq. (16) yields

$$\dot{\sigma}_{yy} = E_{\text{eff}}[\dot{\epsilon}_{\infty} - m c_s b K \rho e^{-(A\rho+\beta)/\tau}] \quad (19a)$$

$$\text{and } \dot{\gamma}_{pl} = c_s b K \rho e^{-(A\rho+\beta)/\tau} \quad (19b)$$

The slip-rate in Eq. (19b) is governed by the dislocation density and its mobility, and is not sensitive to the applied strain-rate. This equation, together with the quantification of dislocation density and resolved shear stress, can provide important insight on the appropriate strain-rates that can be applied for meaningful MD simulation, which are typically constrained by extremely small time-scales. The stress increment in Eq. (19) should decrease during the slip-rate surge stage, typically due to dislocation evolution. However, an opposite trend is observed in the MD simulations, where very high strain-rates ($\sim 10^7$ – 10^9 s^{-1}) approach the maximum slip-rate. This trend is evident in Fig. 2. An applied strain-rate of $\sim 10^9 \text{ s}^{-1}$ leads to a non-physical stress increase in the GPa range. To avoid such stresses, the applied strain rate should be considerably lower than the maximum slip-rate that can be estimated from Eq. (19b).

Fig. 16(a,b) plot the evolution of slip-rate $\dot{\gamma}_{pl}$ as a function of applied strain for lattice orientations 1 and 3 respectively. The model in Eq. (19) is compared with direct MD simulation results in these plots. The results of the simulation are given by the expression:

$$\dot{\gamma}_{pl} = \frac{1}{m} \left[\dot{\epsilon}_{\infty} - \frac{\dot{\sigma}_{yy}}{E_{\text{eff}}} \right] \quad (20)$$

where m is the Schmid factor and E_{eff} is the effective stiffness obtained through unloading. It is evident that the slip-rate surge phenomenon, which governs stress relaxation due to dislocation motion is described very well by the model. The transition behavior from softening to hardening due to loss of dislocation mobility and decrease in resolved shear stress is

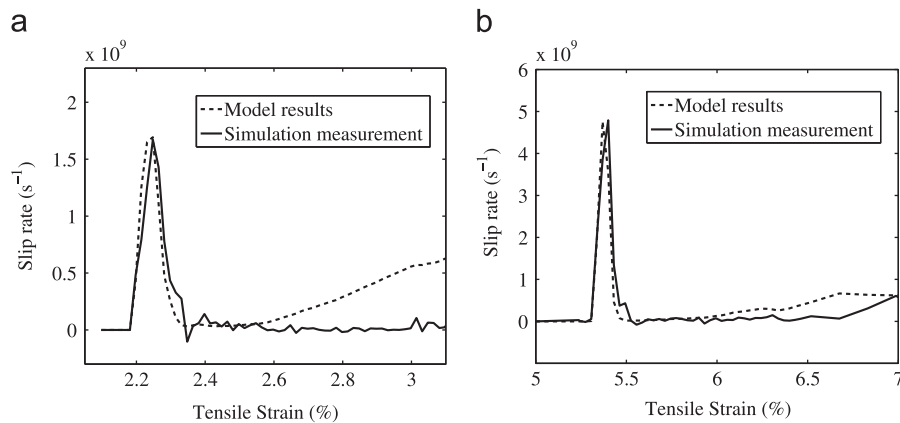


Fig. 16. Comparing the prediction of slip-rate evolution with tensile strain, by the simple model in Eq. (19) and direct MD simulations for (a) lattice orientation 1, and (b) lattice orientation 3.

also adequately captured. Eq. (19) show that the increase in slip-rate comes from nucleation of dislocations while mobility is held fixed. On the other hand, the drop in slip-rate beyond a threshold value is primarily due to the loss of mobility in the dislocation structure, where the formation of a stair-rod dislocation is considered to be important mechanism. The model predictions however diverge from the results of direct MD simulations in the hardening range, mainly on account of overestimating the fraction of mobile dislocations. This could be attributed to the formation of dislocation junctions by multi-slip system interaction, which provides a strong resistance to the dislocation motion. More investigation is needed to find out the local hardening effects at the crack tip due to these high density stair-rod dislocations.

Overall, the concurrence of the mean-field dislocation model with direct MD simulation results provides confidence in the present approach and framework for connecting the evolution of deformation mechanisms with mechanical behavior of crystalline materials in the presence of a crack. The constitutive behavior is however expected to be more involved, coupling deformation and crack propagation laws, if considerable crack evolution occurs in brittle and/or ductile modes.

7. Summary

Modeling crack propagation in crystal plasticity finite element models (CPFEM) for crystalline materials is a challenging enterprise. It has to account for complexities induced by mechanics of the crack, its geometry, crystal lattice orientations, as well as interaction between the propagating crack and a multiplicity of deformation mechanisms such as dislocations, micro-twins, stacking faults etc.. As a first step in this direction, this paper proposes a comprehensive approach based on molecular dynamics simulations of a crystalline material with an embedded crack. The MD platform is selected over other candidate methods such as discrete dislocation dynamics (DDD) to adequately represent the necessary structure of mechanisms and defects, e.g. crack face, twins or even grain boundaries (at a later stage). The approach is aimed at quantitatively connecting deformation mechanisms in the ensemble with the response of the near-crack domain. The MD-based framework invokes a sequence of four tasks to accomplish the overall goal, viz. (i) MD simulation, (ii) characterization of atomic-level crack and deformation mechanisms, (iii) quantification of atomic-level deformation mechanisms and crack, and (iv) response analysis. Effective characterization methods like CNA, DXA and deformation gradient analysis are able to delineate the crack, dislocation structure and micro-twins at a high resolution. Such characterization followed by quantification can facilitate the development of reduced order representations, e.g. evolution of dislocation networks or densities and crack propagation rates, needed for establishing continuum governing laws.

The four-step method is applied to study the effect of relative lattice orientation (with the crack) and Schmid factor on plastic deformation and response in a single crystal nickel system with a center crack, under mode I loading. The strain-rate and system size are carefully selected such that spurious numerical artifacts do not pollute the simulated results. The results reveal that for the Nickel system and loading considered, dislocation nucleation precedes and thwarts cleavage crack propagation upon reaching a critical stress. For certain lattice orientations, dislocation loops are emitted, whereas other orientations favor twin formation due to the nucleation of edge partial dislocations and suppression of cross-slip mechanisms. Stair-rod dislocations form due to dislocation interactions, which serve as pinning points for mobile dislocations and alter the hardening behavior of the system.

Partitioning the total energy of the molecular system into recoverable elastic energy, defect energy and inelastic dissipation, and correlating them with averaged deformation characteristics such as dislocation density and twin volume fraction etc. is an important precursor to the constitutive model development. Analysis results reveal that there is significant difference in the heat conversion ratio for the stages corresponding to twin formation dominated and dislocation dominated deformation.

Finally, a simple mechanistic model of deformation is developed. It accounts for deformation mechanisms in a crystalline material in the presence of a crack. The model associates evolution in dislocation density with the stress–strain response relation. It shows very good quantitative agreement with direct MD simulation results of material softening due to dislocation motion, and adequately captures the transition from softening to hardening behavior. The model can be further used to estimate the range of strain-rates that may be applied for physically meaningful MD simulations. This simple mechanistic model is meant to provide a preliminary understanding of an important part of the overall framework for developing physics-based constitutive models of crystalline materials in the presence of cracks. While the model considered in this study does not reflect the complexities associated with realistic material situations, the results nevertheless provide some confidence in the use of the molecular level framework as a building block to formulate coupled plasticity–damage constitutive models.

A challenge that is encountered with the finite size, MD models is that crack propagation is impeded due to significant plastic deformation caused by dislocation nucleation and evolution near the crack tip. This artifact, caused by the size-scale of the MD models together with applied periodic boundary conditions, prevents the models from realistic representation of material deformation and damage behavior. To mitigate such effects, it is necessary to develop size-dependent, continuum-atomistic self-consistent homogenization methods that will not be constrained by the effects of periodicity, while realizing the effect of evolution in disparate domains. Such methods are currently under consideration and will be reported in future papers.

Acknowledgments

This work has been partially supported by the Air Force Office of Scientific through a STW-21 (Grant # FA9550-09 1 0014, Program Manager: Dr. David Stargel) and by the National Science Foundation, Mechanics and Structure of Materials Program through Grant No. CMMI-1200231 (Program Manager: Dr. Clark Cooper). This sponsorship is gratefully acknowledged.

References

- Ackland, G.J., Jones, A.P., 2006. Applications of local crystal structure measures in experiment and simulation. *Phys. Rev. B* 73, 054104.
- Angelo, J., Moody, N., Baskes, M., 1995. Trapping of hydrogen to lattice defects in nickel. *Modelling Simul. Mater. Sci. Eng.* 3 (3), 289–307.
- Baskes, M.I., 1992. Modified embedded-atom potentials for cubic materials and impurities. *Phys. Rev. B* 46, 2727–2742, <http://dx.doi.org/10.1103/PhysRevB.46.2727>.
- Berendsen, H.J.C., Postma, J.P.M., van Gunsteren, W.F., Dinola, A., Haak, J.R., 1984. Molecular dynamics with coupling to an external bath. *J. Chem. Phys.* 81, 3684–3691.
- Buehler, M., Hartmaier, A., Gao, H., Duchaineau, M., Abraham, F., 2004. Atomic plasticity: description and analysis of a one-billion atom simulation of ductile materials failure. *Comput. Method Appl. M.* 193, 5257–5282.
- Bulatov, V., Cai, W., 2006. *Interfacial Phenomena in Metals and Alloys*. Oxford University Press.
- Camacho, G., Ortiz, M., 1996. Computational modelling of impact damage in brittle materials. *Int. J. Solids Struct.* 33 (20–22), 2899–2938.
- Chassagne, M., Legros, M., Rodney, D., 2011. Atomic-scale simulation of screw dislocation/coherent twin boundary interaction in Al, Au, Cu and Ni. *Acta Mater.* 59 (4), 1456–1463.
- Costanzo, F., Allen, D., 1995. A continuum thermodynamic analysis of cohesive zone models. *Int. J. Eng. Sci.* 33 (15), 2197–2219.
- Daw, M.S., Baskes, M.I., 1984. Embedded-atom method: derivation and application to impurities, surfaces and other defects in metals. *Phys. Rev. B* 29 (12), 6443–6453.
- Dimiduk, D., Uchic, M., Parthasarathy, T., 2005. Size-affected single-slip behavior of pure nickel microcrystals. *Acta Mater.* 53 (15), 4065–4077.
- Gilman, J., 1969. *Micromechanics of Flow in Solids*. McGraw-Hill.
- Gilman, J., Johnston, W., 1962. Dislocations in Lithium Fluoride Crystals. *Solid State Physics*, vol. 13. Academic Press [http://dx.doi.org/10.1016/S0081-1947\(08\)60457-9](http://dx.doi.org/10.1016/S0081-1947(08)60457-9), pp. 147–222.
- Hirth, J.P., Lothe, J., 1982. *Theory of Dislocations*. Krieger Publishing Company.
- Honeycutt, D., Anderson, H., 1987. Molecular dynamics study of melting and freezing of small Lennard–Jones clusters. *J. Chem. Phys.* 91, 4950–4963.
- Horstemeyer, M., Baskes, M.I., Plimpton, S., 2001. Length scale and time scale effects on the plastic flow of fcc metals. *Acta Mater.* 49 (20), 4363–4374.
- Horton, J.A., Ohr, S.M., 1982. TEM observations of dislocation emission at crack tips in aluminium. *J. Mater. Sci.* 17, 3140–3148.
- Hutchinson, J.W., 1976. Bounds and self-consistent estimates for creep of polycrystalline materials. *Proc. R. Soc. Lond. A* 348, 101–127.
- Kadau, K., Germann, T., Lomdahl, P., 2006. Molecular dynamics comes of age: 320-billion-atom simulation on BlueGene/L. *Int. J. Mod. Phys. C* 17, 1755–1761.
- Kelchner, C.L., Plimpton, S.J., Hamilton, J.C., 1998. Dislocation nucleation and defect structure during surface indentation. *Phys. Rev. B* 58, 11085–11088.
- Kibey, S., Liu, J., Johnson, D., Sehitoglu, H., 2007. Predicting twinning stress in fcc metals: linking twin-energy pathways to twin nucleation. *Acta Mater.* 55 (20), 6843–6851.
- Klein, P., Gao, H., 1998. Crack nucleation and growth as strain localization in a virtual-bond continuum. *Eng. Fract. Mech.* 61 (1), 21–48.
- Knap, J., Sieradzki, K., 1999. Crack tip dislocation nucleation in FCC solids. *Phys. Rev. Lett.* 82, 1700–1703.
- Kocks, U.F., Argon, A.S., Ashby, M.F., 1975. Thermodynamics and kinetics of slip. *Prog. Mater. Sci.* 19, 1–300.
- Liu, X., Li, S., Sheng, N., 2008. A cohesive finite element for quasi-continua. *Comput. Mech.* 42, 555–556, <http://dx.doi.org/10.1007/s00466-008-0300-4>. ISSN 0178-7675.
- Mishin, Y., Farkas, D., Mehl, M.J., Papaconstantopoulos, D.A., 1999. Interatomic potentials for monoatomic metals from experimental data and *ab initio* calculations. *Phys. Rev. B* 59, 3393–3407.
- Ohr, S., 1985. An electron microscope study of crack tip deformation and its impact on the dislocation theory of fracture. *Mater. Sci. Eng.* 72 (1), 1–35.
- Olmsted, D., Hector Jr., L., Curtin, W.A., Clifton, R., 2005. Atomistic simulations of dislocation mobility in Al, Ni and Al/Mg alloys. *Modelling Simul. Mater. Sci. Eng.* 13 (3), 371.
- Patil, S.D., Narasimhan, R., Mishra, R.K., 2009. Observation of kink shear bands in an aluminium single crystal fracture specimen. *Scr. Materialia* 61 (5), 465–468, <http://dx.doi.org/10.1016/j.scriptamat.2009.04.043>. ISSN 1359-6462.
- Plimpton, S., 1995. Fast parallel algorithms for short-range molecular dynamics. *J. Comput. Phys.* 117, 1–19.
- Potirniche, G., Horstemeyer, M., Wagner, G., Gullett, P., 2006. A molecular dynamics study of void growth and coalescence in single crystal nickel. *Int. J. Plasticity* 22 (2), 257–278.

- Rice, J.R., 1992. Dislocation nucleation from a crack tip: an analysis based on the Peierls concept. *J. Mech. Phys. Solids* 40 (2), 239–271. [http://dx.doi.org/10.1016/S0022-5096\(05\)80012-2](http://dx.doi.org/10.1016/S0022-5096(05)80012-2). ISSN 0022-5096.
- Spearot, D., Jacob, K., McDowell, D., 2004. Non-local separation constitutive laws for interfaces and their relation to nanoscale simulations. *Mech. Mater.* 36, 825–847.
- Stukowski, A., Albe, K., 2010. Extracting dislocations and non-dislocation crystal defects from atomistic simulation data. *Modelling Simul. Mater. Sci. Eng.* 18 (8), 085001.
- Swygenhoven, H., Derlet, P.M., Froseth, A., 2004. Stacking fault energies and slip in nanocrystalline metals. *Nat. Mater.* 3, 399–403.
- Tadmor, E., Bernstein, N., 2004. A first-principles measure for the twinnability of FCC metals. *J. Mech. Phys. Solids* 52 (11), 2507–2519.
- Tadmor, E., Hai, S., 2003. A Peierls criterion for the onset of deformation twinning at a crack tip. *J. Mech. Phys. Solids* 51 (5), 765–793. ISSN 0022-5096.
- Thompson, N., 1954. Dislocation nodes in face-centred cubic lattices. *Proc. Phys. Soc. B* 66, 481–492.
- Tschopp, M., McDowell, D., 2008. Grain boundary dislocation sources in nanocrystalline copper. *Scripta Mater.* 58 (4), 299–302.
- Tvergaard, V., Hutchinson, J., 1992. The relation between crack growth resistance and fracture process parameters in elastic–plastic solids. *J. Mech. Phys. Solids* 40 (6), 1377–1397.
- Warner, D.H., Curtin, W.A., Qu, S., 2007. Rate dependence of crack-tip processes predicts twinning trends in f.c.c. metals. *Nat. Mater.* 6, 876–881. <http://dx.doi.org/10.1038/nmat2075>.
- Yamakov, V., Saether, E., Phillips, D., Glaessgen, E., 2006. Molecular-dynamics simulation based cohesive zone representation of intergranular fracture processes in aluminum. *J. Mech. Phys. Solids* 54, 1899–1928.
- Yamakov, V., Wolf, D.W., Phillpot, S., Gleiter, H., 2002. Deformation twinning in nanocrystalline Al by molecular-dynamics simulation. *Acta Mater.* 50 (20), 5005–5020.
- Zhou, S.J., Beazley, D.M., Lomdahl, P.S., Holian, B.L., 1996. Large-scale molecular dynamics simulations of three-dimensional ductile failure. *Phys. Rev. Lett.* 78 (3), 479–482.
- Zhou, X., Zimmerman, J., Reedy Jr., E., Moody, N., 2008. Molecular dynamics simulation based cohesive surface representation of mixed mode fracture. *Mech. Mater.* 40, 832–845.
- Zhu, T., Li, J., Yip, S., 2004. Atomistic study of dislocation loop emission from a crack tip. *Phys. Rev. Lett.* 93, 025503.
- Zhu, Y., Wu, X., Liao, X., Narayan, J., Kecskacs, L., Mathaudhu, S., 2011. Dislocation-twin interactions in nanocrystalline fcc metals. *Acta Mater.* 59 (2), 812–821. ISSN 1359-6454.
- Zimmerman, J., Bammann, D., Gao, H., 2009. Deformation gradients for continuum mechanical analysis of atomistic simulations. *Int. J. Solids Struct.* 46 (2), 238–253. ISSN 0020-7683.
- Zimmerman, J., Gao, H., Abraham, F., 2000. Generalized stacking fault energies for embedded atom FCC metals. *Modelling Simul. Mater. Sci. Eng.* 8 (2), 103.